Encapsulation Effects on Ge-Rich GeSbTe Phase-Change Materials at High Temperature

Oumaima Daoudi, Emmanuel Nolot, Mélanie Dartois, Magali Tessaire, François Aussenac, Nicolas Bernier, Nicolas Gauthier, Névine Rochat, Frédéric Fillot, Van-hoan Le, et al.

Encapsulation effects on Ge-rich GeSbTe Phase-Change Materials at high temperature

Oumaima Daoudi, *Emmanuel Nolot**, *Mélanie Dartois*, *Magali Tessaire*, *François Aussenac*, *Nicolas Bernier*, *Nicolas Gauthier*, *Névine Rochat*, *Frédéric Fillot*, *Van-Hoan Le*, *Hubert Renevier*, and *Gabriele Navarro**

O. Daoudi, E. Nolot, M. Dartois, M Tessaire, F. Aussenac, N. Bernier, N. Gauthier, N. Rochat, F. Fillot, V-H. Le, and G. Navarro

Univ. Grenoble Alpes, CEA, Leti, F-38000 Grenoble, France

Email Address: gabriele.navarro@cea.fr / emmanuel.nolot@cea.fr

H. Renevier

Univ. Grenoble Alpes, CNRS, LMGP, F-38000, Grenoble, France-G-INP

Keywords: *Phase-Change Memories, Ge-rich GeSbTe, Encapsulation, Interfaces, High temperature*

Ge-rich GeSbTe chalcogenide alloys have gained significant attention in the field of phase-change materials due to their remarkable thermal stability and thus their suitability for integration in non-volatile memories targeting embedded automotive applications. In this study we focus on the effects of different encapsulating materials on the evolution and on the crystallization kinetic of N-doped Ge-rich GeSbTe films. These films are annealed with temperatures compatible with the Back-End-of-Line (BEOL) of the CMOS fabrication. First, we show how the encapsulation layer thickness should be tuned in order to protect the layer from oxidation and at the same time to avoid delamination phenomena. We compare TaN, C, TiN, SiC and SiN used as encapsulating layers. The segregation and crystallization of Ge-rich GeSbTe alloys appear more homogeneous in the case of C, TiN and SiC. On the contrary we observe the effects of an interfacial heterogeneous nucleation in the case of TaN and SiN. It results in a different final morphology of the chalcogenide layer after annealing depending on the encapsulation, with different grain sizes and kinetic of phase separation.

1 Introduction

Phase-Change Memory (PCM) has demonstrated its maturity in terms of scalability, fast programming speed and high endurance with respect to all the other emerging non-volatile memory technologies [1]. Furthermore, today PCM can also ensure the high thermal stability and the reliability required in embedded automotive applications. This was possible thanks to the material engineering of the well known Ge-Sb-Te ternary system [2], employing Ge-rich stoechiometries and light elements doping (e.g. Nitrogen) [3, 4, 5].

The effects of oxidation on the phase-change properties were analyzed in common chalcogenide layers such as GeTe and $Ge_2Sb_2Te_5$ in particular highlighting the reduction of the crystallization temperature [6]. Equivalent effects were observed with the presence of oxygen in the encapsulating layer (eL) with a promotion of the interfacial heterogeneous nucleation [7]. Such phenomenon becomes more critical in Ge-rich GeSbTe (GGST) systems since Ge is highly subject to oxidation [8]. Indeed, under air exposure, Ge atoms tend to bond to oxygen atoms at the GGST surface creating a Ge-O layer leading to the formation of an underneath Te-rich region. This region acts as seed for the phases segregation (i.e. crystalline cubic Ge and cubic GeSbTe phase) into the rest of the layer at high temperature [9]. This confirms the importance of preventing or at least slowing down the oxidation in GGST layers to preserve their integrity and structural evolution once exposed to the thermal budget of the device integration. Moreover, it becomes fundamental to understand the possible interactions and effects that metals and dielectrics used in the integration process could have once co-integrated with GGST alloys.

In this work, we investigate the effects of different encapsulating layers used in the integration of PCM devices, on the N-doped GGST (GGST) structural evolution at high temperature. We compare the results obtained without encapsulation (i.e. air exposed samples) with GGST layers encapsulated with thin layers of Carbon (C), Tantalum

Nitride (TaN), Titanium Nitride (TiN), Silicon Nitride (SiN) and Silicon Carbide (SiC), after annealing steps up to 500 °C. TiN, C and TaN are commonly used as electrodes in PCM devices and integrated after the chalcogenide layer deposition [10, 11, 12, 13, 14], while SiN and SiC are used as encapsulating layers after the etching of phase-change layer [15].

We followed the evolution of the samples combining several complementary techniques: Fourier-Transform InfraRed (FTIR) and Raman spectroscopies, X-Ray Diffraction (XRD) and Transmission Electron Microscopy (TEM) equipped with Energy Dispersive X-ray (EDX). We show how the thickness of the encapsulating layer, especially in the case of C and TaN, needs to be optimized to achieve a balance between avoiding both oxidation stress-induced phenomena. The crystallization kinetic of GGST appears homogeneous and not affected by the eL up to 400 °C, except for TaN that induces the Ge heterogeneous nucleation and crystallization at the eL/GGST interface. At higher temperature, the surface oxidation in the case of ultra-thin C layer and the surface heterogeneity in the case of SiN, lead respectively to a preferential Ge segregation at the eL/GGST interface, similarly to what is observed with TaN with a significant grain growth. We think that these results contribute to the evaluation of the best encapsulating solutions and of their effects for the investigation of GGST in the case of fundamental physico-chemical analyses and to the understanding of the phenomena that could affect the chalcogenide layer properties during the PCM fabrication process.

2 Materials and methods

N-doped GGST layers were deposited on 300 mm Si(100) wafers by reactive magnetron co-sputtering from Ge and $Ge_2Sb_2Te_5$ targets at low temperature, under constant Ar/N_2 gas flow within the deposition chamber in order to tune N doping. The encapsulation of the chalcogenide layer was performed by sputtering technique at 70 °C in the same deposition tool (*in situ*) in the case of C, TaN and TiN, while it was performed *ex situ* by PECVD (Plasma Enhanced Chemical Vapor Deposition) process in the case of SiC and SiN layers at 320 °C and 350 °C, respectively. We kept for comparison a GGST sample without encapsulation (i.e. air exposed). The thicknesses and deposition temperatures of different encapsulating layers are summarized in **Table 1**.

The as-deposited samples were annealed (*ex situ*) at different temperatures up to 500 °C with a ramp-up of 10 °C/min and for the duration of 5 minutes at the target temperature under inert N_2 atmosphere. Raman spectra were acquired at room temperature using a Renishaw InVia Raman spectrometer. A 532 nm laser diode served as the excitation source, using a focusing lens with a magnification of 100x and a numerical aperture of 0.85. The measurements were performed in the Raman shift range of 100 cm^{-1}-1000 cm^{-1}. To prevent heating and unwanted crystallization of the samples, the laser power was maintained at 0.12 mW.

XRD data were obtained at room temperature using a PANalytical Empyrean two-circle diffractometer. Cu$K\alpha$ radiation ($\lambda = 1.5406$ Å) was employed as X-ray source. The measurements were carried out in Bragg-Brentano geometry within the 2θ range of 20°-60°.

FTIR spectra were recorded in the wavenumber range of 4000 cm^{-1}-30 cm^{-1} (Bruker Vertex 70V) with a resolution of 4 cm^{-1}, by accumulating 64 scans. FTIR spectra were analyzed in particular in the 600 cm^{-1}-1000 cm^{-1} wavenumber range, by performing Lorentzian deconvolution of the main features.

For TEM-EDX analyses, we utilized Ga^+ Focused Ion Beam (FIB) milling to prepare the samples. Silicon oxide and tungsten protection layers were deposited to shield the region of interest from the ion beam tails. Observation took place at 200 kV using a Titan Themis FEI microscope with probe correction, equipped with the Super-X detector system for EDX. EDX mappings were generated at a resolution of 320x900 pixels with a dwell time of 50 µs.

3 Effects of the encapsulation layer thickness on crystallization kinetic of GGST

C, TaN and TiN are commonly used as electrodes in PCM device fabrication, and they are integrated immediately after the chalcodenide layer (favorably *in situ*, as in our case). Thus, it is important to tune their thickness in order to preserve the layer from oxidation while simulteneously avoid stress phenomena that can be detrimental for the layer integrity. As TiN is well known in integration and already optimized, we focused on C and TaN for the

exploration of the impact of the thickness. The thickness of SiN and SiC eLs have been chosen to be compatible with standard device process.

In agreement with previous analyses performed on GGST layers [16], by *in situ* ellipsometry (**Fig. S1** in Supplementary Materials) we extracted the crystallization temperature (T_c) of the GGST samples observing the change in optical behavior with increasing temperature and we report the extracted T_c in Table 1.

3.1 Carbon encapsulation

FTIR spectroscopy was used to investigate N-doped GGST layers encapsulated with different thicknesses of C layer: 5, 10 and 20 nm. In GGST alloys, Nitrogen bonds mainly with Ge atoms, resulting in the formation of Ge-N features [3, 5, 17, 18, 19, 20]. The presence of a significant charge transfer from Ge to N leads to the overlap of distinct and pronounced bands. IR spectra for the three samples before (as-deposited) and after annealing at 500 °C are shown in **Figure 1**. The prominent absorption band located at 700 cm^{-1} in the as-deposited samples and associated with the in-plane asymmetric stretching vibration of the Ge_3N skeleton group [21], is shifted toward higher wavenumeber values ($\sim$ 750 cm^{-1}) after annealing. This shift is attributed to the rearrangement of the Ge and N atoms in more stable Ge-poorer Ge-N atomic structures, with the release of Ge atoms that thus participate to the growth of the cubic Ge phase [3]. The shift of the Ge-N main peak becomes more important when decreasing the C eL thickness, while the intensity of the feature attributed to germanium oxide (Ge-O) [22, 23] increases **Figure 2**. Such a behavior starts at about 350 °C for 5 nm thick C eL and at 400 °C for 10 nm thick eL, while for the 20 nm eL it does not appear up to 500 °C, confirming the preservation of the GGST layer.

The Raman spectra of the three samples annealed at 400 °C are shown in **Figure 3**. They exhibit three main bands [3] summarized below and in **Table 2**:

- Below 150 cm^{-1} the features are attributed to the vibrational modes of Ge-Te bonds [24];
- The peak at 154 cm^{-1} is attributed to the stretching mode of $SbTe_3$ pyramidal units (Sb-Te bonds) present in GeSbTe system [25, 26];
- The third part of the spectra, covering the wavenumber range 190 cm^{-1}-300 cm^{-1}, corresponds to Ge-Ge vibrational modes. The peaks at 230 cm^{-1} and 270 cm^{-1} are attributed respectively to the LO (longitudinal optical) and TO (transverse optical) vibrational modes of amorphous germanium (a-Ge). The position and the broadness of these peaks suggest that the Ge atoms are arranged in an amorphous disordered structure [27, 28]. The sharp peak at about 300 cm^{-1} is attributed to the vibrational modes of crystalline germanium (c-Ge) [28].

The sample encapsulated with a 5 nm thick C layer shows the presence of c-Ge at 400 °C and a reorganization of Ge-Te and Sb-Te bonds compatible with the crystallization of a GeSbTe phase, whereas the other samples remain amorphous. This difference can be attributed to the acceleration of the crystallization mechanism due to the surface oxidation as observed in FTIR analyses. The crystallization in the samples covered with thick C eL starts at higher temperature (inset of Figure 3). Ge-C interactions (see **Fig. S3** in Supplementary Materials) and Ge-O formation at the eL/GGST interface at high temperatures (above $\sim$ 425 °C) could influence the crystallization dynamic into the layer explaining the different c-Ge peak development.

3.2 TaN encapsulation

Hereafter we report on the effect of TaN eL thickness on the crystallization of GGST layer. After annealing at 500 °C a 10 nm eL induces delamination at the top and bottom interfaces, while the 5 nm thick eL preserves the sample integrity (**Figure 4**). The observed stress could be explained by the different thermal expansion coefficients (CTE) of Ge and TaN during crystallization, with values respectively of 7.5×10^{-6} $°C^{-1}$ and 6.6×10^{-6} $°C^{-1}$ at 400 °C [29, 30].

TEM-EDX analyses of 10 nm TaN eL (see **Fig. S4** in Supplementary Materials) reveales a thin oxide layer, certainly unduced by delamination.

The crystallization of the GGST layer with TaN eL begins at lower temperature ($\sim$ 380 °C) with respect to other eLs, as revealed by ellipsometry measurements (Table 1). The evolution of the area of the Raman c-Ge peak peak with annealing temperature shows a dependency between thickness and crystallization temperature(**Figure 5**), 350 °C in the case of 5 nm TaN eL and at about 380 °C in the case of 10 nm TaN eL. For blanket deposition, the 5 nm thick TaN proved to be more reliable than 10 nm thick one as it prevents oxidation and delamination.

It's worth noting that in a real device integration, the TaN electrode is patterned before exposing the material to a high-temperature thermal budget. This implies that even thicker TaN electrodes can be integrated with a reduced risk of layer delamination after the patterning step.

4 Effects of encapsulation layer on GGST crystallization kinetic

In this section, we compare the evolution of crystallization kinetics in the GGST layer with different eLs: C 20 nm, TaN 5 nm, TiN 20 nm, SiN 20 nm and SiC 20 nm eLs.

FTIR analyses: a focus on Ge-N features:

Figure 6 presents the IR spectra of GGST samples after annealing at 400 °C, showing the Ge-N main features between a-Ge_3N_x and Ge-N positions at 700 cm^{-1} and 750 cm^{-1}, respectively. The shift of Ge-N peak position differs within the evaluated eLs, with a larger shift corresponding to an increased release of Ge atoms from the Ge-N group. The largest shift is obtained with TaN eL, showing an advanced evolution of GGST with respect to the one in the other samples. **Figure 7** shows the increase of the Ge-N peak position with annealing temperature. Both TiN and C cases exhibit a similar gradual increase in position. The contrast in trend with the other encapsulations becomes particularly evident at 400 °C. Note that the Ge-N shift in SiC and SiN sample is already visible at room temperature, due to the higher deposition temperature (> 320 °C). All the samples show a stable position of the Ge-N peak at about 750 cm^{-1} at 500 °C.

Raman analyses: a focus on c-Ge peak:

We performed Raman analyses on the samples annealed at increasing temperatures. The c-Ge peak area appears higher in TaN eL with respect to the other samples (**Figure 8**), confirming the role of TaN in enhancing the Ge crystallization. The c-Ge peak is already present at 400 °C in SiN and SiC eLs, likely due to their higher deposition temperature as previously highlighted, while it is absent for TiN and C. At 500 °C, SiC and TiN exhibit lower crystallization progress, with a slight difference attributed to the variation in deposition temperature. On the other hand, SiN demonstrates a more advanced crystallization progress compared to SiC. TEM-EDX section indicates that this is certainly a result of heterogeneous nucleation.

XRD analyses: crystallization evolution upon annealing:

XRD analyses allow to further investigate the development of the Ge and GeSbTe crystalline phases in GGST (**Figure 9**). At 400 °C, we observe that the C and TiN encapsulated samples remain amorphous, in agreement with Raman analyses (Figure 8), whereas with TaN eL the GGST layer exhibits well defined Bragg peaks corresponding to cubic fcc Ge (Fd-3m) and cubic fcc GeSbTe (Fm-3m) crystalline phases. As observed in Raman analyses, SiN shows an advancement of the crystallization, in particular for c-Ge, that is comparable with air exposed sample. The XRD patterns for C and TiN eLs do not present any peak, meaning that GGST layer is still amorphous.

In **Figure 10** we report the Ge crystallites size as a function of the annealing temperature. TaN is confirmed to enhance the Ge crystallization even at higher temperature with respect to the other samples. At 500 °C the Ge grains size has a steep increase for SiN eL, while in the other samples the grain sizes remains in the 10 nm range. Furthermore, the GST grains (**Fig. S5** in Supplementary Materials) present larger size than Ge grains as already

reported in the litterature [16].

TEM-EDX analyses: morphology of GGST layer at 500 °C:

We support the previous results with TEM/EDX images obtained from samples annealed at 500 °C (see **Figure 11**). The TiN and SiC encapsulated GGST samples exhibit an homogeneous distribution of the two crystalline phases (Ge and GeSbTe), segregated within the layer. On the contrary, we observe in the case of the 5 nm thick C eL a Ge enrichment at the eL/GGST interface that features heterogeneous nucleation due to the incoming oxidation, (section IIIA). SiN eL leads to larger Ge-rich region. In the case of TaN eL and air-exposed samples, we observe a bi-layer morphology.

5 Discussion

The combination of different techniques reveals that TiN serves as an effective encapsulating layer, preventing from oxidation, delamination, and resulting in a homogeneous morphology after complete crystallization at 500 °C. This homogeneity is also observed in the case of SiC, with the difference that crystallization is slightly enhanced compared to TiN due to the higher deposition temperature (Figure 8).

TaN exhibits an advanced crystallization compared to other eLs. The crystallization process favors Ge crystallization at the top interface with large crystallite sizes (Figure 10), while the GeSbTe phase crystallizes in the bottom part of the GGST layer (Figure 11c). This is in line with recent studies demonstrating the chemical interaction between Ta and Ge, promoting Ge reorganization towards a crystalline phase [31]. On the other hand, in the case of air exposed samples, GGST exhibits an accumulation of Ge atoms at the sample surface, implicated in the oxidation process (Ge-O), resulting in an underlying Te-rich zone [9]. The segregation of the GeSbTe phase initiates in this zone, allowing Ge to crystallize and grow at the bottom. This gives rise to a bi-layer structure with a cubic GeSbTe crystalline phase at the top and a cubic Ge phase at the bottom (Figure 11a).

The 5 nm C eL shows as well heterogeneities at 500 °C, possibly because, at this temperature, the thin C eL is fully diffused in the chalcogenide, exposing the layer to air and leading to oxidation. This favors heterogeneous nucleation and lead to low crystallization temperature (Figure 3). In comparison, for 20 nm C eL no oxidation effects are observed in FTIR analyses (Figure 2), thus we expect an homogeneous layer after annealing, compatibly with TiN or SiC eL.

In the case of SiN eL, XRD analyses reveal an enhanced Ge crystallization growth at 500 °C, consistent with TEM/EDX analyses (Figure 11e). As reported previously for $Ge_2Sb_2Te_5$ [32], the SiN layer accelerates the crystallization growth rate, particularly at high temperatures [33].

6 Conclusion

In this work, we presented a thorough investigation of the effects of different encapsulation layers on N-doped Ge-rich GeSbTe materials structural evolution at high temperature, combining a wide set of techniques such as Raman and FTIR spectroscopy, XRD and TEM/EDX analyses. The thickness of C eL should be increased up to 20 nm in order to ensure the layer protection from oxidation up to 500 °C, while TaN thickness should be sufficiently reduced in order to avoid stress-induced delamination phenomena during the GGST crystallization at high temperature. Moreover, TaN eL highly enhances the Ge crystallization likely due to the Ta-Ge chemical interaction inducing Ge heterogeneous nucleation at the TaN interface. C, TiN and SiC do not affect the crystallization dynamic of GGST layers upon annealing. SiN demonstrated similar performances, even if it enhancese the c-Ge growth above 450 °C. Our results contribute to the understanding of the different possible scenarios of GGST segregation and crystallization, and to help the design of PCM devices integrating this alloy.

Supporting Information

Supporting Information is available from the Wiley Online Library or from the author.

Acknowledgements

Part of this work, carried out on the Platform for NanoCharacterisation (PFNC) of CEA, was supported by the "Recherche Technologique de Base" Program of the French National Research Agency (ANR). It was partially funded by European commission, French State and Auvergne-Rhône-Alpes region through ECSEL-IA 101007321 project StorAIge and within the frame of the IPCEI Microelectronics.

References

[1] P. Cappelletti, R. Annunziata, F. Arnaud, F. Disegni, A. Maurelli, P. Zuliani, *Journal of Physics D: Applied Physics* **2020**, *53*.

[2] S. Raoux, F. Xiong, M. Wuttig, E. Pop, *MRS Bulletin* **2014**, *39* 703.

[3] L. Prazakova, E. Nolot, E. Martinez, F. Fillot, D. Rouchon, N. Rochat, M. Bernard, C. Sabbione, D. Morel, N. Bernier, A. Grenier, A.-M. Papon, M.-C. Cyrille, G. Navarro, *Journal of Applied Physics* **2020**, *128*, 21 215102.

[4] P. Zuliani, E. Palumbo, M. Borghi, G. Dalla Libera, R. Annunziata, *Solid-State Electronics* **2015**, *111* 27.

[5] I. Yang, K. Do, H.-J. Chang, D.-H. Ko, H. Sohn, *J. Electrochem. Soc.* **2010**, *157*, 4 H483.

[6] E. Gourvest, B. Pelissier, C. Vallée, A. Roule, S. Lhostis, S. Maitrejean, *Journal of The Electrochemical Society* **2012**, *159*, 4 H373.

[7] P. Noé, C. Sabbione, N. Bernier, N. Castellani, F. Fillot, F. Hippert, *Acta Materialia* **2016**, *110* 142.

[8] M. Agati, C. Gay, D. Benoit, A. Claverie, *Applied Surface Science* **2020**, *518* 146227.

[9] L. Goffart, B. Pelissier, G. Lefèvre, Y. Le–Friec, C. Vallée, G. Navarro, J. Reynard, *Applied Surface Science* **2022**, *573* 151514.

[10] A. Verdy, G. Navarro, M. Bernard, S. Chevalliez, N. Castellani, E. Nolot, J. Garrione, P. Noé, G. Bourgeois, V. Sousa, M.-C. Cyrille, E. Nowak, In *2018 IEEE International Reliability Physics Symposium (IRPS)*. **2018** .

[11] K. Ren, X. Duan, Q. Xiong, Y. Li, S. Lv, Z. Song **2019**, *30*, 22 20037.

[12] L. Perniola, P. Noé, Q. Hubert, S. Souiki, G. Ghezzi, G. Navarro, A. Cabrini, A. Persico, V. Delaye, D. Blachier, J.-P. Barnes, E. Henaff, M. Tessaire, E. Souchier, A. Roule, F. Fillot, J. Ferrand, A. Fargeix, F. Hippert, J.-Y. Raty, C. Jahan, V. Sousa, G. Torelli, S. Maitrejean, B. De Salvo, G. Reimbold, In *2012 International Electron Devices Meeting*. **2012** .

[13] J. Wu, M. Breitwisch, S. Kim, T. Hsu, R. Cheek, P. Du, J. Li, E. Lai, Y. Zhu, T. Wang, H. Cheng, A. Schrott, E. Joseph, R. Dasaka, S. Raoux, M. Lee, H. Lung, C. Lam, ISBN 978-1-4577-0505-2, **2011** .

[14] A. L. Serra, G. Lefevre, O. Cueto, G. Bourgeois, M. C. Cyrille, G. Navarro, E. Nowak, *Solid-State Electronics* **2021**, *186* 108111.

[15] C. De Camaret, G. Bourgeois, O. Cueto, V. Meli, S. Martin, D. Despois, V. Beugin, N. Castellani, M. Cyrille, F. Andrieu, J. Arcamone, Y. Le-Friec, G. Navarro, In *ESSDERC 2022 - IEEE 52nd European Solid-State Device Research Conference (ESSDERC)*. **2022** 233–236.

[16] L. Prazakova, E. Nolot, E. Martinez, D. Rouchon, F. Fillot, N. Bernier, R. Elizalde, M. Bernard, G. Navarro, *Materialia* **2022**, *21* 101345.

[17] B. Liu, Z. Song, T. Zhang, J. Xia, S. Feng, B. Chen, *Thin Solid Films* **2005**, *478*, 1 49.

[18] E. Nolot, C. Sabbione, W. Pessoa, L. Prazakova, G. Navarro, *Applied Surface Science* **2021**, *536* 147703.

[19] K.-H. Kim, J.-C. Park, J.-H. Lee, J.-G. Chung, S. Heo, S.-J. Choi, *Japanese Journal of Applied Physics* **2010**, *49*, 10 101201.

[20] K. B. Borisenko, Y. Chen, S. A. Song, D. J. H. Cockayne, *Chemistry of Materials* **2009**, *21*, 21.

[21] A. Zanatta, I. Chambouleyron, *Physical Review B* **1993**, *48*, 7 4560.

[22] V. Tolstoy, I. Chernyshova, V. Skryshevsky, *Handbook of Infrared Spectroscopy of Ultrathin Films* **2003**.

[23] G. Maggioni, S. Carturan, L. Fiorese, N. Pinto, F. Caproli, D. R. Napoli, M. Giarola, G. Mariotto, *Applied Surface Science* **2017**, *393* 119.

[24] K. Andrikopoulos, S. Yannopoulos, G. Voyiatzis, A. Kolobov, M. Ribes, J. Tominaga, *Journal of Physics Condensed Matter* **2006**, *18*.

[25] K. S. Andrikopoulos, S. N. Yannopoulos, A. V. Kolobov, P. Fons, J. Tominaga, *Journal of Physics and Chemistry of Solids* **2007**, *68*, 5 1074.

[26] P. Němec, A. Moreac, V. Nazabal, M. Pavlišta, J. Přikryl, M. Frumar, *Journal of Applied Physics* **2009**, *106*, 10 103509.

[27] P. Kazimierski, J. Tyczkowski, M. Kozanecki, Y. Hatanaka, T. Aoki, *Chemistry of Materials* **2002**, *14*, 11 4694.

[28] H. Jamali, R. Mozafarinia, A. Eshaghi, *Journal of Alloys and Compounds* **2015**, *646* 360.

[29] P. Hidnert, *Bureau of Standards Journal of Research* **1929**, *2*, 5.

[30] V. Yang, M. Groenert, C. Leitz, A. Pitera, M. Currie, E. Fitzgerald, *Journal of Applied Physics* **2003**, *93* 3859.

[31] C. Kopas, S. Zhang, J. Gonzales, D. R. Queen, B. Wagner, R. W. Carpenter, N. Newman, Ge thin-films with tantalum diffusion-barriers for use in nb-based superconductor technology, **2021**.

[32] N. Ohshima, *Journal of Applied Physics* **1996**, *79*, 11 8357.

[33] K. Cil, Y. Zhu, J. Li, C. Lam, H. Silva, *Thin Solid Films* **2013**, *536* 216.

Table 1: Summary of the encapsulating layers explored. The crystallization temperatures (T_c) of the N-doped GGST samples were extracted from ellipsometry measurements (not reported). The T_c reported for TaN and C was measured respectively for a thickness of 5 nm and 20 nm.

Encapsulating layer	Deposition temperature (°C)	Thickness (nm)	T_c (°C)
Air exposed	-	-	411
TaN	$\sim$ 70 (*in situ*)	5/10	380
C	$\sim$ 70 (*in situ*)	5/10/20	416
TiN	$\sim$ 70 (*in situ*)	20	419
SiN	$\sim$ 320 (*ex situ*)	20	412
SiC	$\sim$ 350 (*ex situ*)	20	417

Table 2: Main features of the GGST Raman spectra.

Band position	Attribution	References
$\sim$ 154 cm^{-1}	$SbTe_3$ pyramidal units	[25, 26]
$<$ 150 cm^{-1}	GeTe-based features	[24]
190 cm^{-1}-300 cm^{-1}	190 cm^{-1}-300 cm^{-1}: amorphous germanium (a-Ge)	[27, 28]
	$\sim$ 300 cm^{-1}: crystalline germanium (c-Ge)	[28]

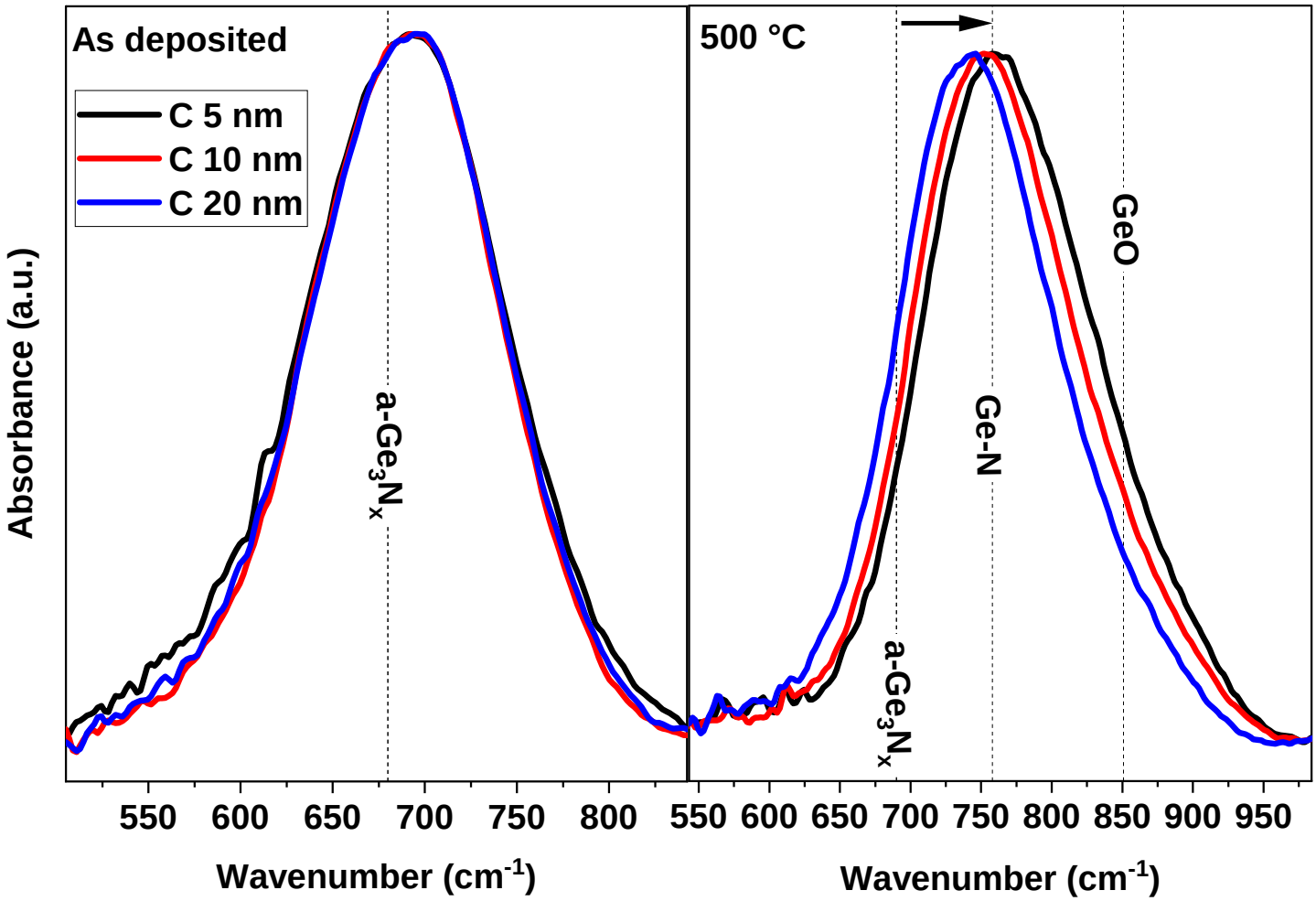

Figure 1: FTIR spectra of GGST samples encapsulated with C layers of different thicknesses (5, 10 and 20 nm) before (left) and after annealing at 500 °C (right). The amorphous a-Ge_3N_x peak is considered to be the main one in as-deposited samples and it shifts toward higher wavenumbers after annealing. The deconvolution of as-deposited and annealed IR spectra is present in **Figure. S2** in the Supplementary Materials.

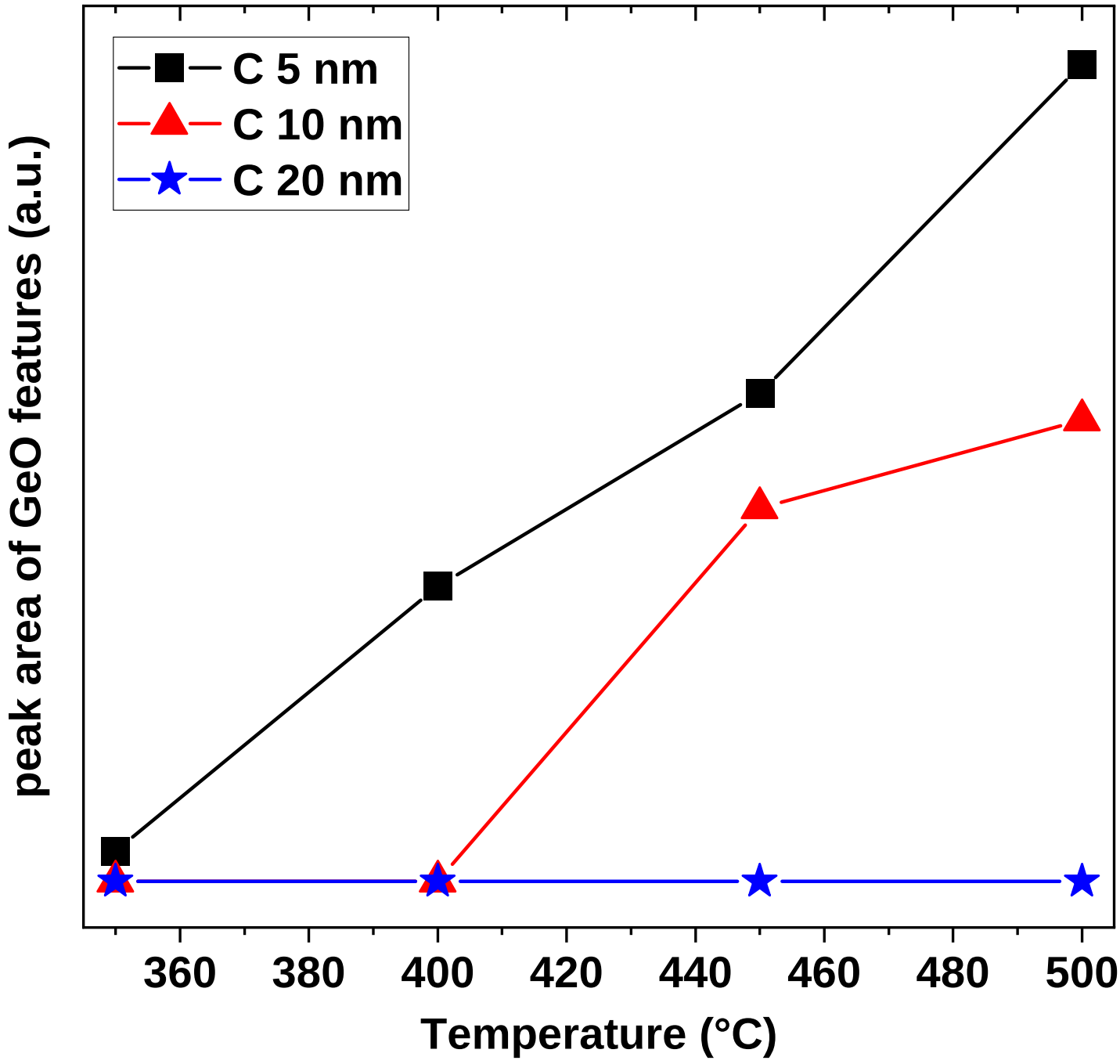

Figure 2: Peak area evolution of Ge-O feature (obtained after deconvolution of FTIR spectra) from 350 °C to 500 °C for different thicknesses of C eL.

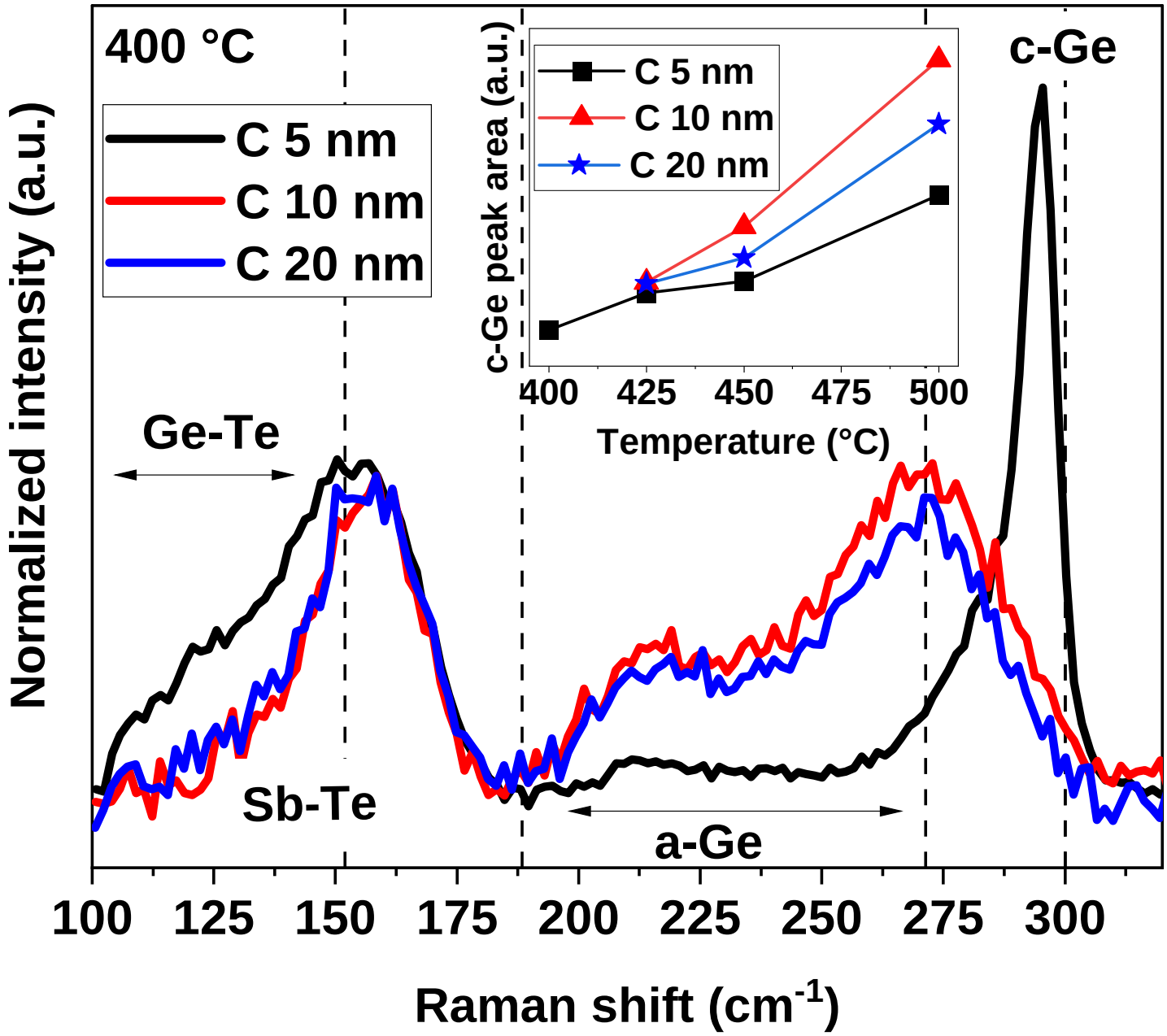

Figure 3: Raman spectra of GGST samples encapsulated with different C layer thicknesses annealed at 400 °C. The inset shows the evolution at increasing annealing temperatures of c-Ge peak area.

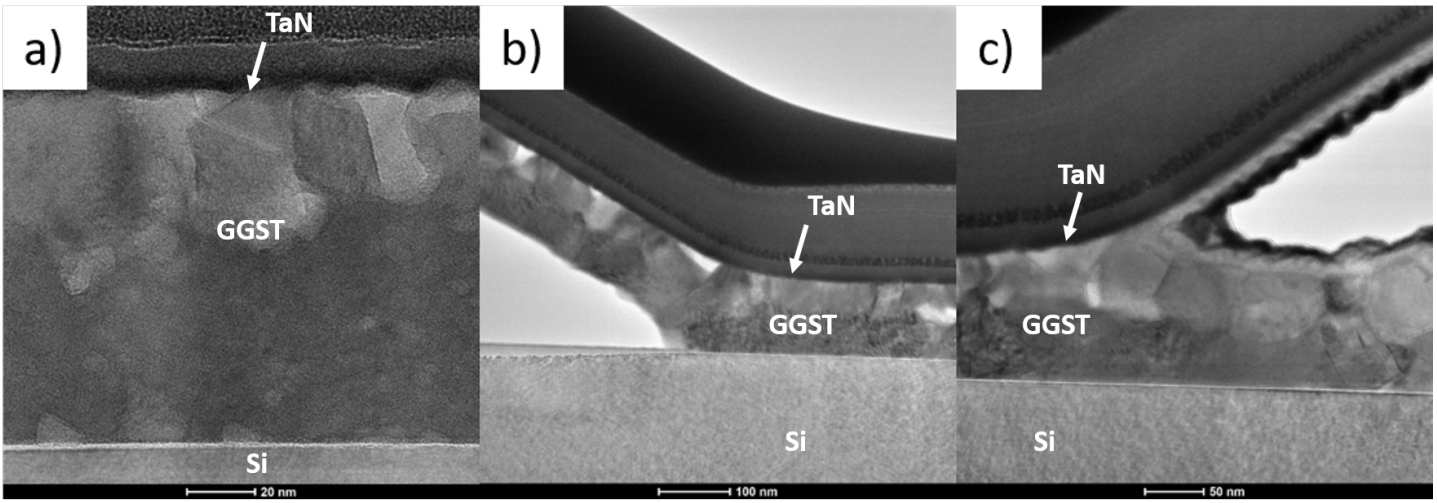

Figure 4: TEM analyses of GGST samples with TaN eL after annealing at 500 °C. The 5 nm-TaN eL (a) preserves the GGST layer integrity, while the 10 nm-TaN eL induces delamination at the GGST/substrate (b) or at the eL/GGST interface (c).

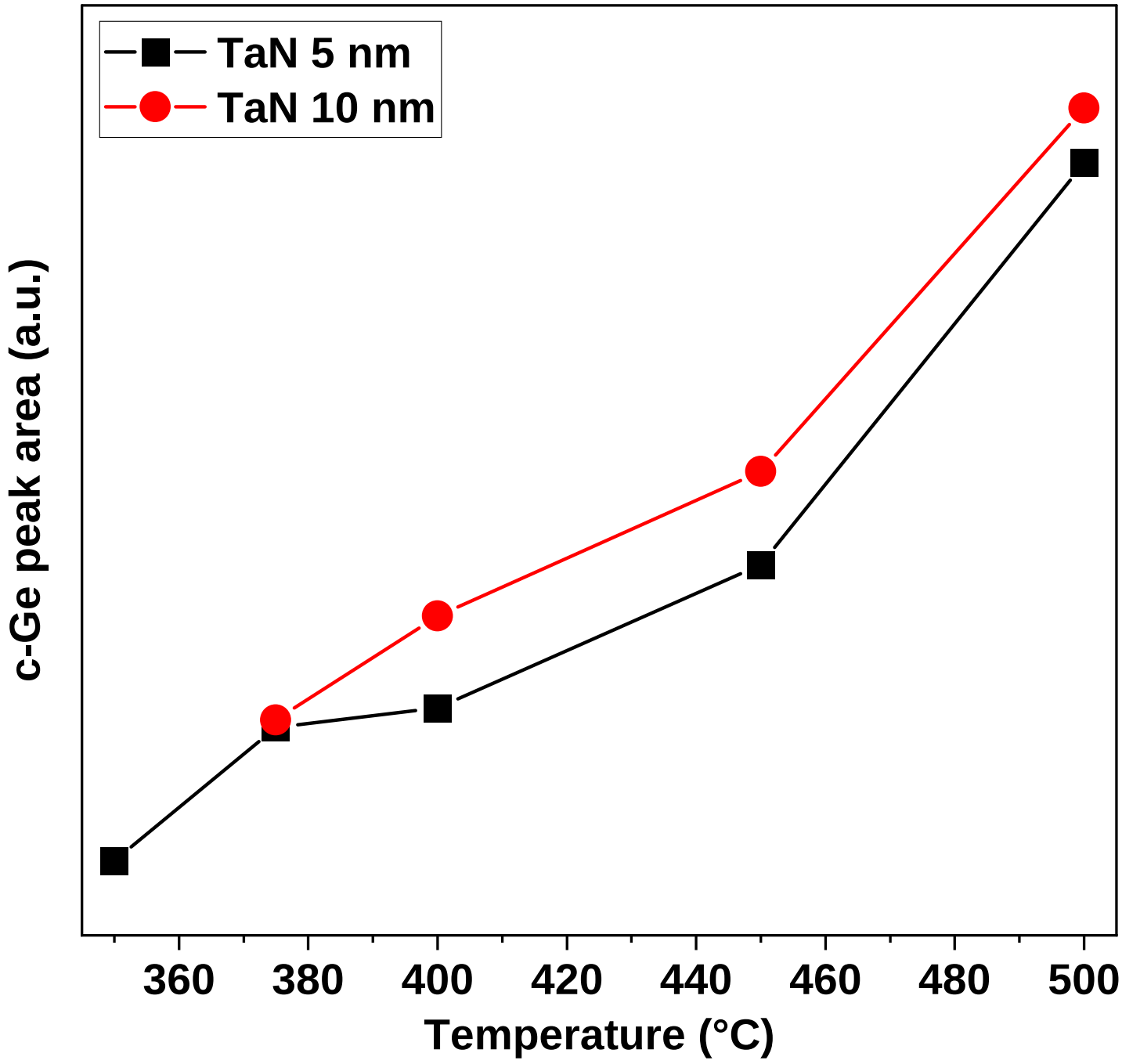

Figure 5: Peak area evolution of c-Ge peak extracted from Raman spectra of GGST samples encapsulated with TaN eL and at increasing annealing temperature from 350 °C to 500 °C.

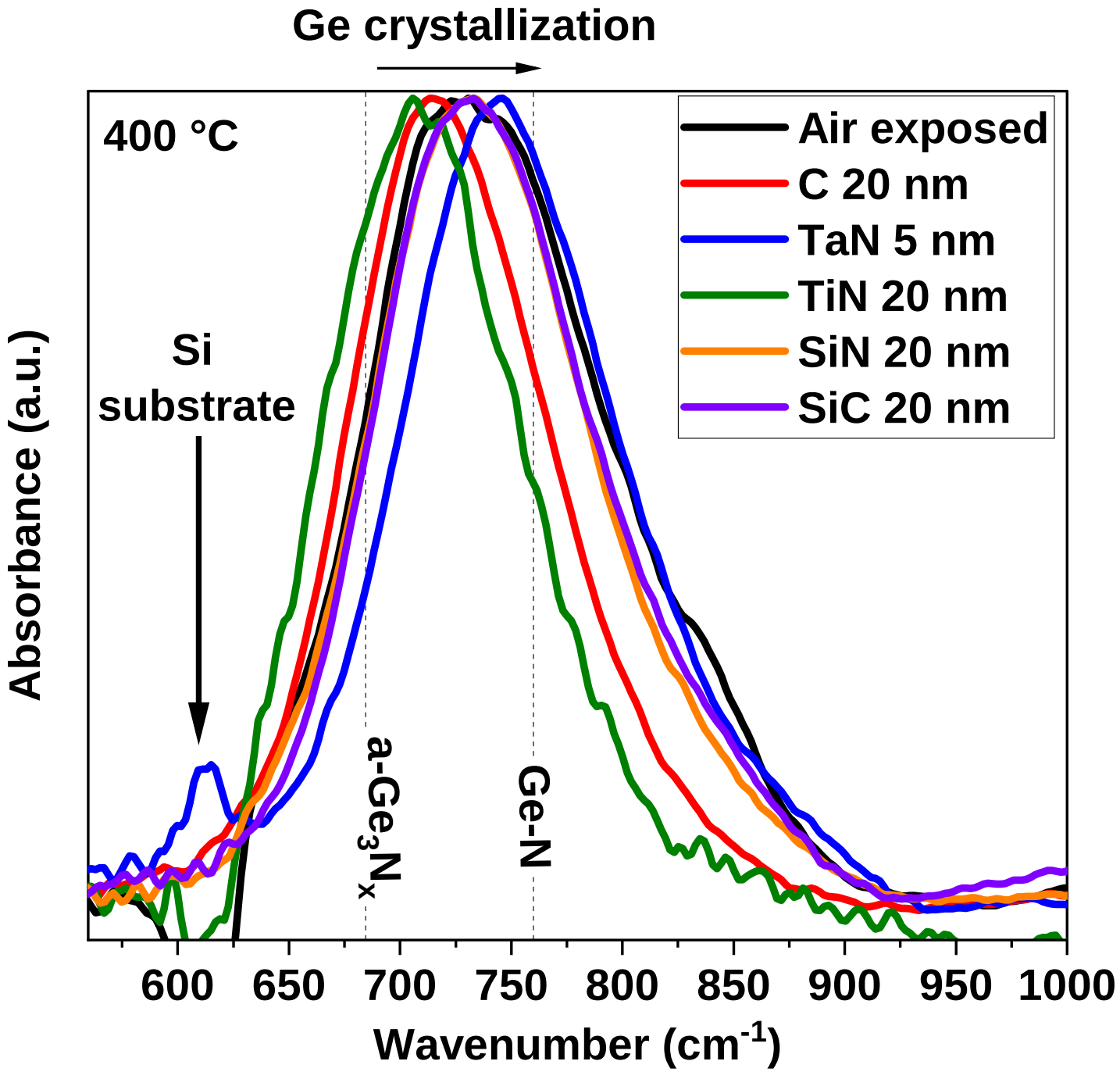

Figure 6: IR spectra of GGST samples after annealing at 400 °C.

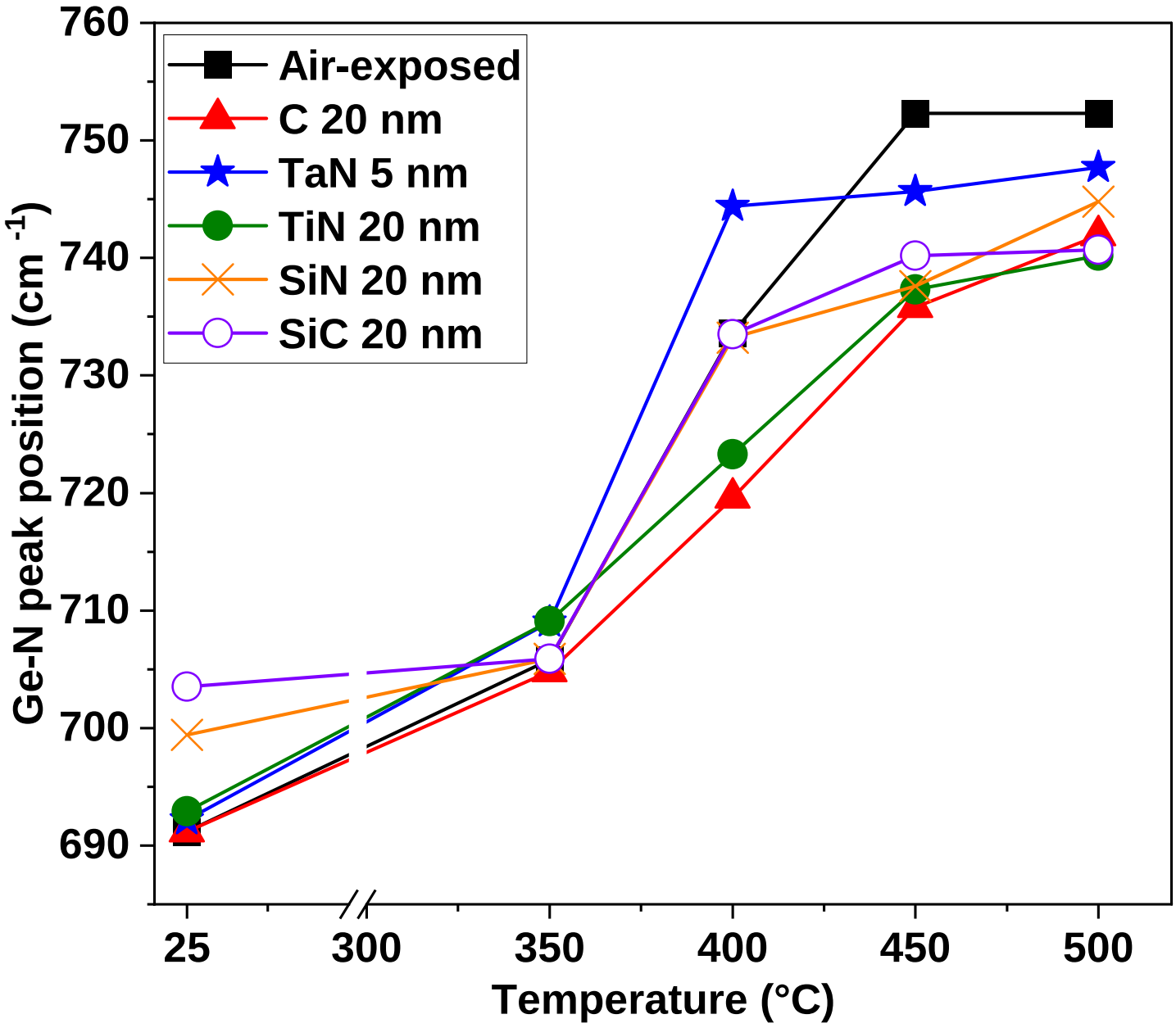

Figure 7: Evolution of Ge-N peak position extracted from FTIR spectra for all the samples as a function of the annealing temperature.

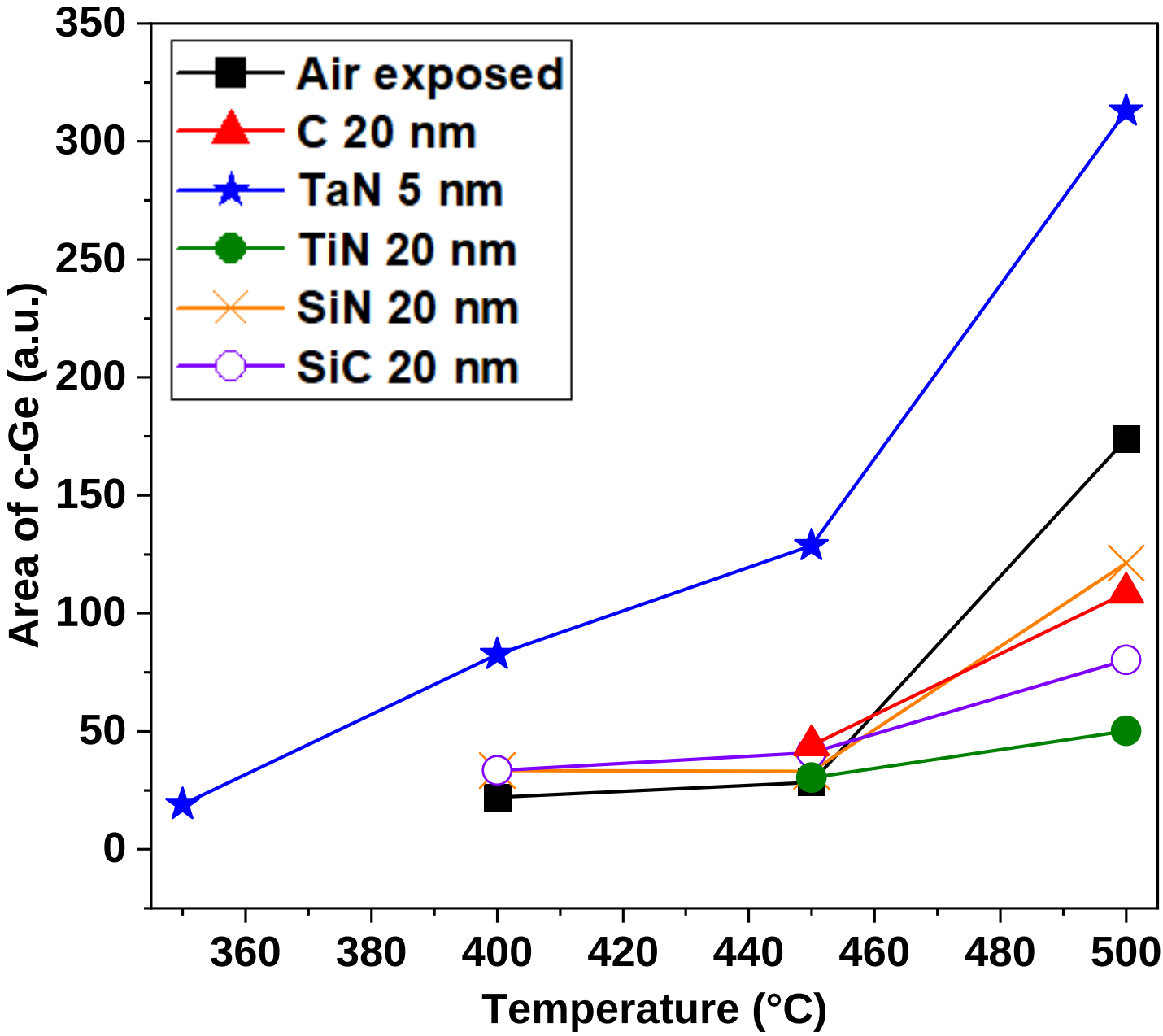

Figure 8: Evolution of c-Ge peak area obtained from Raman spectra at increasing annealing temperature.

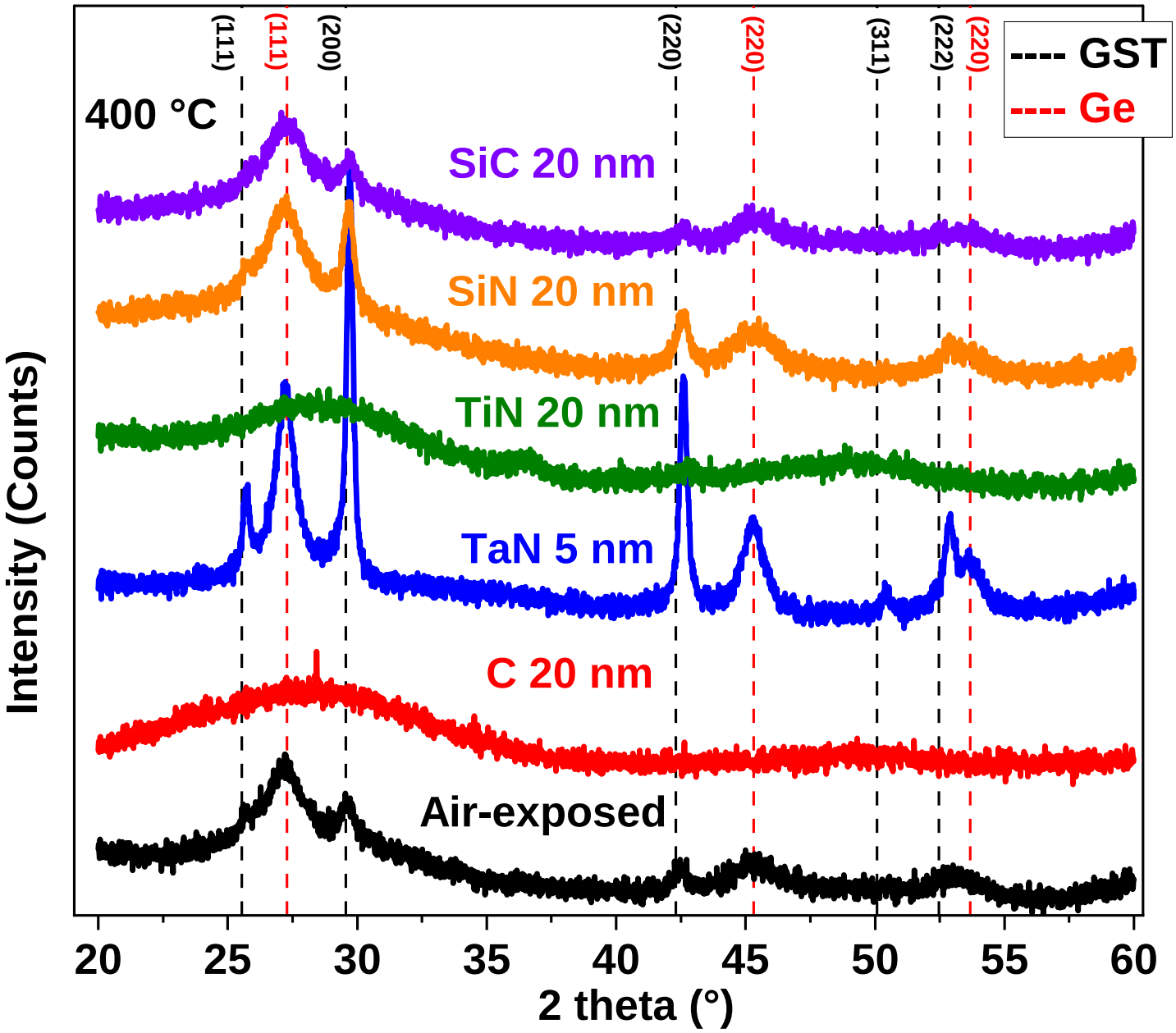

Figure 9: XRD patterns of GGST layers after annealing at 400 °C. Indexation is performed from database data (ICDD PDF Nos. 00-054-0484 and 00-004-0545).

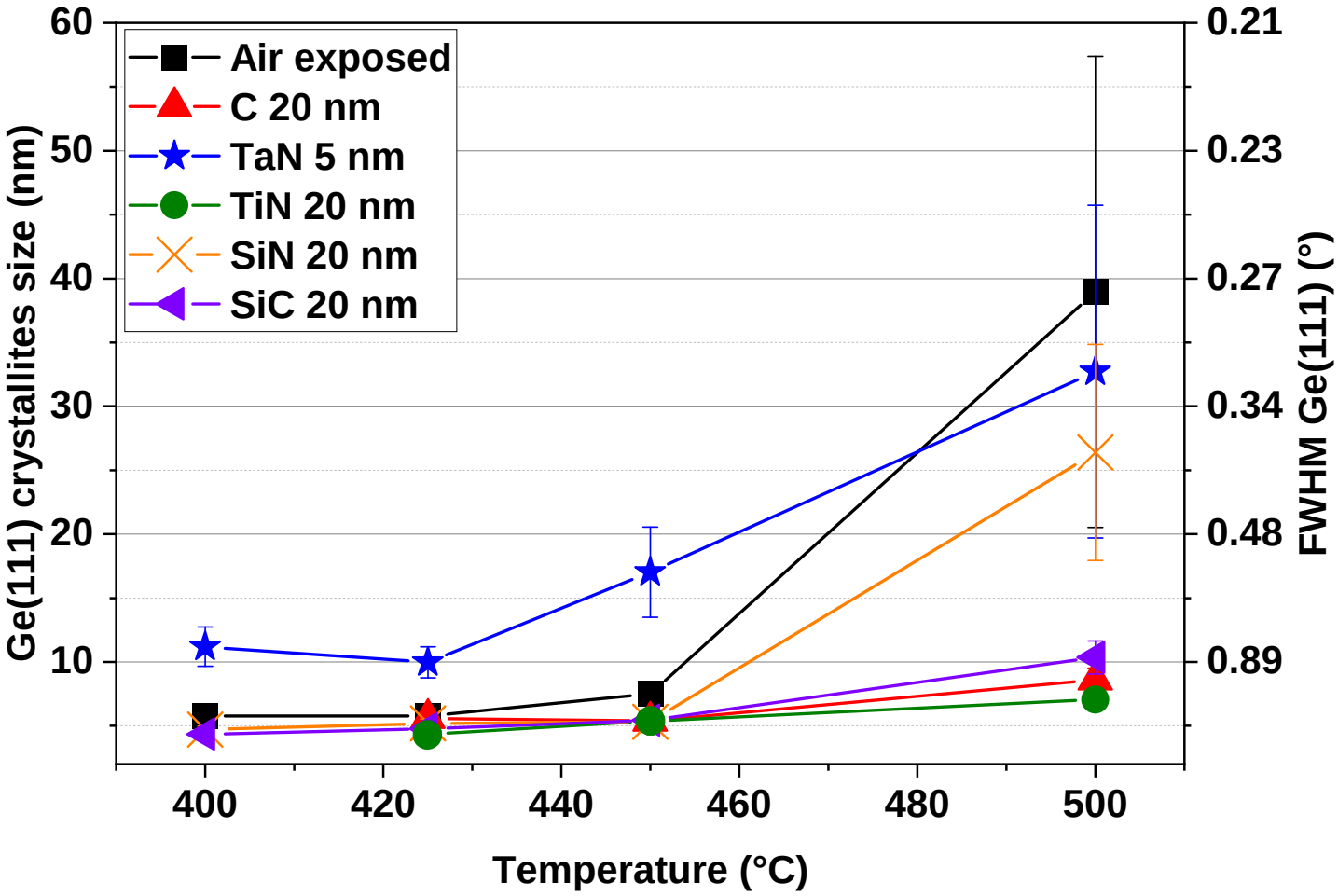

Figure 10: Crystallites size calculated from Scherrer's law for the Ge phase, considering the Ge (111) Bragg main peak in XRD patterns (at about $2\theta = 26°$, as shown in Figure 9) obtained from the samples annealed at increasing temperature.

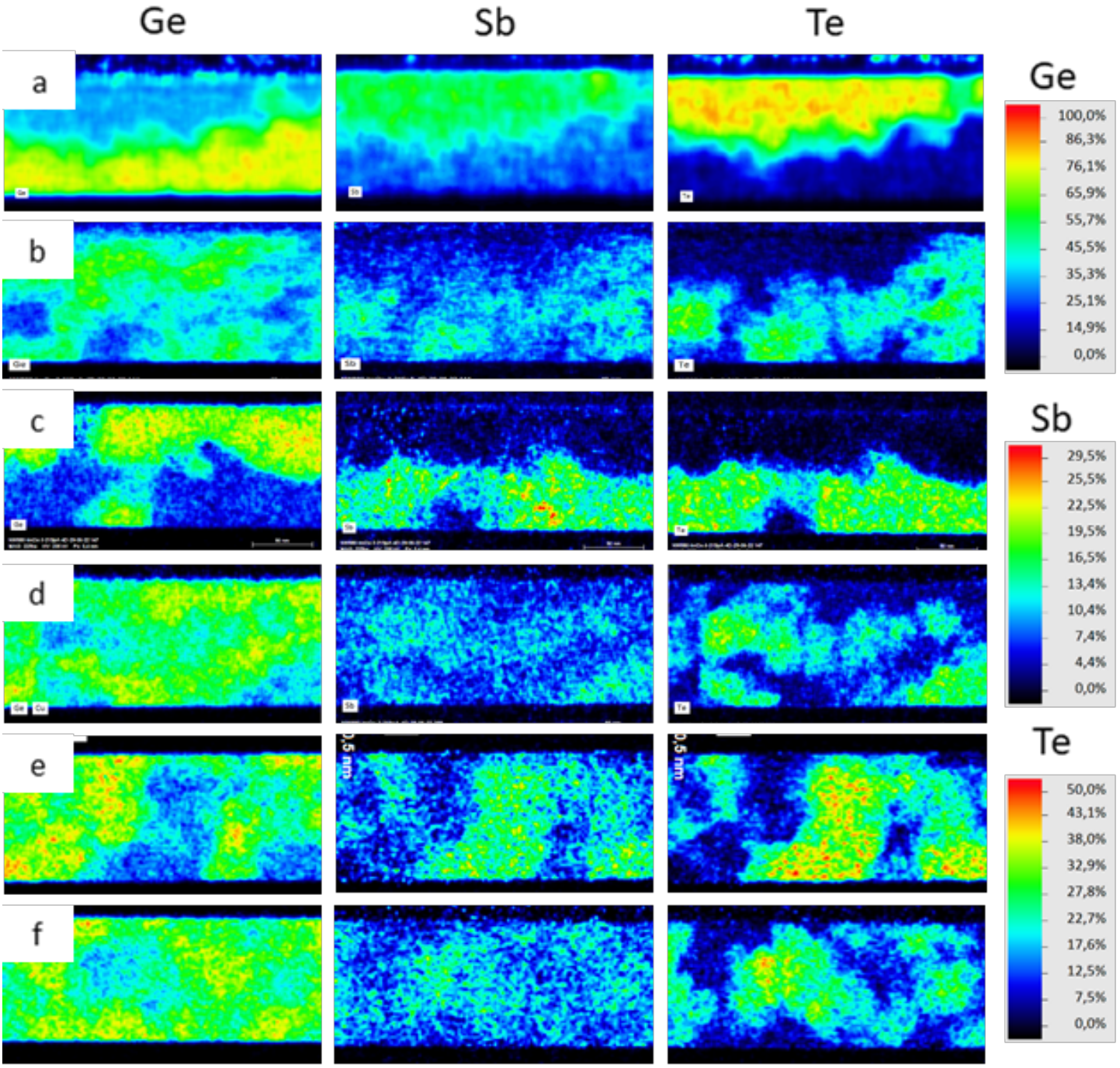

Figure 11: TEM/EDX images display the elementary compositions of GGST layers after annealing at 500 °C with different encapsulations: (a) air exposed, (b) C 5 nm, (c) TaN 5 nm, (d) TiN 20 nm, (e) SiN 20 nm, (f) SiC 20 nm.